Interplay of excitonic effects and van Hove singularities in optical spectra: CaO and AlN polymorphs

A. Riefer,[*] F. Fuchs, C. Rödl, A. Schleife, and F. Bechstedt

Institut für Festkörpertheorie und -optik, Friedrich-Schiller-Universität and European Theoretical Spectroscopy Facility (ETSF), Max-Wien-Platz 1, 07743 Jena, Germany

R. Goldhahn

Institut für Experimentelle Physik, Otto-von-Guericke-Universität, Universitätsplatz 2, 39106 Magdeburg, Germany

The quasiparticle band structures and fundamental energy gaps of the rock-salt (rs), zinc-blende (zb), and wurtzite (wz) polymorphs of CaO and AlN are calculated within the G_0W_0 approximation on top of a self-consistent solution of the generalized Kohn–Sham equation with the hybrid functional HSE03. Based on these reliable electronic structures, the dielectric functions of rs-CaO, zb-AlN, and wz-AlN including excitonic effects are obtained from the solution of the Bethe–Salpeter equation. The peaks and structures in the absorption spectra are analyzed in terms of critical points in the joint band structure and the joint density of states. We find that some features of the optical absorption can be clearly assigned to bound excitonic states located at M_0 or M_1 critical points, while others are merely due to a large joint density of states.

I. INTRODUCTION

For about 12 years, optical absorption spectra of simple bulk semiconductors and insulators could be calculated from first principles taking the full quasiparticle (QP) band structure and the excitonic and local-field effects into account.[1–3] The approach is based on many-body perturbation theory:[4] The macroscopic optical polarization function is obtained from the solution of a Bethe–Salpeter equation (BSE) to account for the electron-hole pair interactions,[5–7] while the many-body influence on the single-particle level is described by solving the QP equation[4,8–10] with an exchange-correlation (XC) self-energy in Hedin's GW approximation.[11] Meanwhile, the theory has been generalized to spin-polarized systems.[12] Nowadays, optical spectra including excitonic effects can be calculated not only for bulk semiconductors and insulators[1–3] but also for solid surfaces,[13–15] molecules,[16,17] and nanocrystals.[18–20] Moreover, the accuracy of the method has been improved significantly so that even exciton binding energies of only a few millielectron volts can be computed or predicted.[21–24] However, open questions remain, e.g., with respect to the dynamics of the screening and the contribution of the lattice polarizability.[25]

The influence of many-body effects in bulk systems becomes manifest in some general features of the optical absorption spectra:[1,2,12] (i) Going from the independent-particle approximation (IPA) to the independent-QP approximation[26] (IQPA), the optically excited noninteracting electron-hole pairs are replaced by noninteracting quasi-electron–quasi-hole pairs, thus accounting for the interaction of the individual electrons or holes with the gas of valence electrons. This usually leads to a remarkable blueshift of the spectrum toward higher photon energies in accordance with the opening of the QP gap. Thereby, the modifications of the overall line shape are normally small (see, e.g., Ref. 27). (ii) The inclusion of the screened electron-hole attraction via the BSE approach leads to a redshift of the IQPA absorption spectrum apart from

the absorption edge itself. It is accompanied by a sometimes drastic redistribution of oscillator strength from higher to lower photon energies. On the other hand, the local-field effects are of minor influence for many bulk semiconductors and insulators. (iii) In many systems, e.g., direct semiconductors or insulators, the absorption edge is significantly modified by the formation of bound excitonic states.[21–23,25] They are characterized by absorption peaks within the fundamental QP gap and, hence, finite binding energies. Their oscillator strengths are usually increased due to the Coulomb enhancement. In addition, the spectral strength of the scattering states above the fundamental gap is also enhanced, which can be described by the Sommerfeld factor in the Wannier–Mott model.[28]

In the early days of semiconductor physics, enormous progress in the understanding of the electronic structures was achieved by a simplifying identification procedure: Peaks and shoulders in the imaginary part of the frequency-dependent dielectric function were attributed to van Hove singularities of type M_0, M_1, M_2, or M_3 in the joint density of states (JDOS), which later became the standard textbook interpretation[28–30] of optical spectra. Van Hove singularities occur at so-called critical points $\mathbf{k}_{\rm cr}$ in the Brillouin zone (BZ) where the gradient of the difference between conduction (c) and valence (v) QP bands $\varepsilon_{c\mathbf{k}}^{\rm QP} - \varepsilon_{v\mathbf{k}}^{\rm QP}$ vanishes. It has been argued that these energy differences $\varepsilon_{c\mathbf{k}_{\rm cr}}^{\rm QP} - \varepsilon_{v\mathbf{k}_{\rm cr}}^{\rm QP}$ are measured by means of many modulation spectroscopy techniques.[29] However, the experience theoreticians gained over the last years concerning the influence of excitonic effects on the absorption spectra renders the simple interpretation of spectral features solely by means of van Hove singularities questionable. State-of-the-art *ab initio* many-body calculations ask at least for a more careful interpretation of the spectra in terms of QP band structures, on the one hand, and excitonic effects, on the other hand.[31] Now, the accuracy reached in the computation of band structures and Coulomb interaction matrix elements allows such a careful analysis.

In the present paper, we aim for a detailed understanding of the optical absorption spectra of CaO and AlN and a critical discussion of the origin of occurring absorption peaks. Both materials are strongly ionic with high-charge asymmetry coefficients g: Following the chemical trend of CaSe and CaS,[32] a value of $g > 0.906$ can be estimated for CaO. For AlN in the zinc-blende (*zb*) structure, $g = 0.794$ has been found.[32] The anions are first-row elements with nearly equal and small covalent radii $r_O = 0.73$ Å and $r_N = 0.75$ Å.[33] The covalent radii of the cations, on the other hand, differ a lot from each other, i.e., $r_{Ca} = 1.74$ Å and $r_{Al} = 1.18$ Å.[33] As a consequence,[34] CaO and AlN crystallize in different crystal structures with different atomic coordination. While CaO usually exhibits a sixfold coordination in the cubic rock-salt (*rs*) structure,[35] AlN is fourfold coordinated. Its equilibrium geometry is the hexagonal wurtzite (*wz*) structure,[35] but deposited AlN layers also show the cubic *zb* structure.[36] For purpose of comparison, we investigate both compounds, CaO and AlN, within the *rs*, *zb*, and *wz* crystal structures. Additionally, CaO is studied in the hexagonal B_k-BN structure.

The paper is organized as follows. In Sec. II, we briefly compile the applied theoretical methods and specify the computational details. In Sec. III, the ground-state properties and the QP band structures are presented. The results for the optical absorption spectra are given in Sec. IV. The influence of the excitonic effects and the validity of the critical-point analysis are discussed in detail. Section V deals with the excitons near the band edges. Finally, a short summary is given in Sec. VI.

II. THEORETICAL AND COMPUTATIONAL METHODS

The ground-state properties of the crystal polymorphs of CaO and AlN are calculated within density functional theory[37,38] (DFT) as implemented in the Vienna *Ab-initio* Simulation Package[39] (VASP). The interaction of the valence electrons (Ca $3s$, Ca $3p$, Ca $4s$, O $2s$, and O $2p$ for CaO or Al $3s$, Al $3p$, N $2s$, and N $2p$ in the case of AlN) with the cores is described by means of the projector-augmented wave (PAW) method.[40] The wave functions are expanded in plane-wave basis sets with cutoff energies of 350 eV. For the ground-state calculations, the generalized-gradient approximation (GGA) in the parametrization of Perdew, Burke, and Ernzerhof[41] (PBE) is used. The face-centered cubic (*fcc*) and the hexagonal BZs are sampled by Γ-centered meshes with $8 \times 8 \times 8$ or $8 \times 8 \times 6$ **k** points, respectively. For unit cells with internal degrees of freedom, the positions of the ions are relaxed until the Hellmann–Feynman forces are below 5 meV/Å. The minimum of the total energy with respect to the volume is obtained by means of a fit to the Murnaghan equation of state.[42] For the calculation of the cohesive energies, we have subtracted the spin-polarized ground-state energies of the free atoms.

The QP bands are determined by a perturbative solution of the QP equation[8] with the XC self-energy in the GW approximation.[8,11] The iteration starts with a self-consistent solution of a QP equation, sometimes also called a generalized Kohn–Sham (KS) equation, with a self-energy derived from the nonlocal HSE03 hybrid functional[43] (zeroth order). Subsequently, the GW corrections are calculated in first-order perturbation theory, i.e., within the so-called one-shot G_0W_0

approach[9,10,44] (for details of the implementation see Ref. 45). In addition, we present QP eigenvalues calculated in the G_0W_0 approach on top of the PBE ground-state electronic structures. For the computation of the QP band structures, $8 \times 8 \times 8$ **k** points and 150 bands were used for the cubic polymorphs. In the case of the hexagonal structures, $8 \times 8 \times 6$ **k** points and 300 bands were necessary for both materials to converge the band energies with an accuracy of 0.1 eV.

The macroscopic dielectric function $\varepsilon(\omega)$ is obtained by solving the BSE for spin-singlet excitations including the attractive screened electron-hole interaction and an exchange-like term accounting for the local-field effects.[6,7] To this end, the BSE is transformed into an eigenvalue problem for an effective two-particle Hamiltonian:

$$\sum_{c'v'\mathbf{k}'} \hat{H}(cv\mathbf{k}, c'v'\mathbf{k}') \, A_\Lambda(c'v'\mathbf{k}') = E_\Lambda \, A_\Lambda(cv\mathbf{k}). \quad (1)$$

The eigenvalues E_Λ represent the electron-hole pair excitation energies which are labeled by the quantum numbers Λ. The eigenvectors $A_\Lambda(cv\mathbf{k})$ are the electron-hole pair amplitudes or mixing coefficients of optical single-particle transitions. The excitonic electron-hole pair Hamiltonian[1,4] reads

$$
\begin{aligned}
\hat{H}(cv\mathbf{k}, c'v'\mathbf{k}') = & \left(\varepsilon_{c\mathbf{k}}^{QP} - \varepsilon_{v\mathbf{k}}^{QP} \right) \delta_{cc'} \, \delta_{vv'} \, \delta_{\mathbf{k}\mathbf{k}'} \\
& - \int d\mathbf{r} \int d\mathbf{r}' \, \varphi_{c\mathbf{k}}^*(\mathbf{r}) \, \varphi_{c'\mathbf{k}'}(\mathbf{r}) \\
& \times W(\mathbf{r},\mathbf{r}') \, \varphi_{v\mathbf{k}}(\mathbf{r}') \, \varphi_{v'\mathbf{k}'}^*(\mathbf{r}') \\
& + 2 \int d\mathbf{r} \int d\mathbf{r}' \, \varphi_{c\mathbf{k}}^*(\mathbf{r}) \, \varphi_{v\mathbf{k}}(\mathbf{r}) \\
& \times \bar{v}(\mathbf{r} - \mathbf{r}') \, \varphi_{c'\mathbf{k}'}(\mathbf{r}') \, \varphi_{v'\mathbf{k}'}^*(\mathbf{r}'). \quad (2)
\end{aligned}
$$

The first term describes the noninteracting quasi-electron–quasi-hole pairs. The second term accounts for the screened electron-hole Coulomb attraction with the statically screened Coulomb potential $W(\mathbf{r},\mathbf{r}')$. The third contribution, governed by the nonsingular part of the bare Coulomb interaction $\bar{v}(\mathbf{r} - \mathbf{r}')$, represents the electron-hole exchange or crystal local-field effects. The matrix elements of the potentials are calculated by means of the single-particle wave functions $\varphi_{n\mathbf{k}}(\mathbf{r})$, with the band index n running over valence or conduction bands. With the solution of Eq. (1), the frequency-dependent macroscopic dielectric function can be written as

$$
\begin{aligned}
\varepsilon(\hat{\mathbf{q}},\omega) = & 1 + \frac{8\pi e^2}{V} \sum_\Lambda \left| \sum_{cv\mathbf{k}} M_{\hat{\mathbf{q}}}(cv\mathbf{k}) \, A_\Lambda^*(cv\mathbf{k}) \right|^2 \\
& \times \left[\frac{1}{E_\Lambda - \hbar(\omega + i\eta)} + \frac{1}{E_\Lambda + \hbar(\omega + i\eta)} \right], \quad (3)
\end{aligned}
$$

with $\hat{\mathbf{q}}$ being the unit vector in the direction of light incidence and η the pair damping constant. The crystal volume is given by V. The optical transition matrix elements are evaluated in the longitudinal approach,[46]

$$M_{\hat{\mathbf{q}}}(cv\mathbf{k}) = \lim_{\mathbf{q} \to 0} \frac{1}{|\mathbf{q}|} \int d\mathbf{r} \, \varphi_{c\mathbf{k}}^*(\mathbf{r}) \, e^{i\mathbf{q}\mathbf{r}} \, \varphi_{v\mathbf{k}-\mathbf{q}}(\mathbf{r}). \quad (4)$$

To save computational work load, an analytical expression,[47] which depends on the electronic static dielectric constant $\varepsilon(\omega = 0) = \varepsilon_\infty$ and the average valence-electron density, is employed to describe the screening of the electron-hole

attraction in W. For the dielectric constants, values of $\varepsilon_\infty = 3.89$ (rs-CaO), $\varepsilon_\infty = 4.75$ (zb-AlN), and $\varepsilon_\infty = 4.66$ (wz-AlN, average over Cartesian directions) have been obtained within the IPA using PBE eigenvalues and single-particle wave functions.

The investigation of the fine structure of optical absorption spectra, especially near the absorption edge and for low-energy optical transitions, requires finer **k**-point samplings than those necessary for the ground-state calculations. For the fcc structures, we apply a Γ-centered $18 \times 18 \times 18$ mesh, while in the hexagonal case a Γ-centered $14 \times 14 \times 12$ mesh is used. Further, a sufficiently large number of conduction bands has to be included in the calculations to describe the electron-hole pair interaction properly. The number of empty states is limited by introducing a cutoff energy for the electron-hole single-particle transitions (without QP corrections) that contribute to the excitonic Hamiltonian of Eq. (2). The cutoff of 20 eV applied here is sufficient to converge the structures occurring in the imaginary part of the dielectric function in the spectral range discussed throughout this paper.

The matrix elements of the excitonic Hamiltonian have been evaluated by means of DFT-PBE wave functions. Since the usage of PBE+G_0W_0 QP eigenvalues still leads to a gap underestimation (see Sec. III B), HSE03+G_0W_0 eigenvalues are employed instead of PBE+G_0W_0 eigenvalues on the main diagonal of the Hamiltonian. It has been carefully checked that no change of band ordering occurs when going from PBE to HSE03. For even finer meshes up to $40 \times 40 \times 40$ **k** points in the case of AlN (see Sec. IV B), also the calculation of QP shifts in the G_0W_0 approach becomes unaffordable. However, the comparison of HSE03+G_0W_0 and HSE03 eigenvalues (see Sec. III B) indicates that the application of a scissors operator,[9] i.e., a constant shift Δ^{QP} of the conduction bands toward higher energies, gives good agreement of the HSE03+G_0W_0 and HSE03+Δ^{QP} band structures.

The huge size of the excitonic Hamiltonian matrix of Eq. (2) prohibits a direct diagonalization. For this reason, the dielectric functions are computed by means of an efficient time-evolution scheme.[14,27] Compared with a direct diagonalization, this approach scales as $\mathcal{O}(N^2)$ instead of $\mathcal{O}(N^3)$, with N being the number of pair states, i.e., the rank of the Hamiltonian.
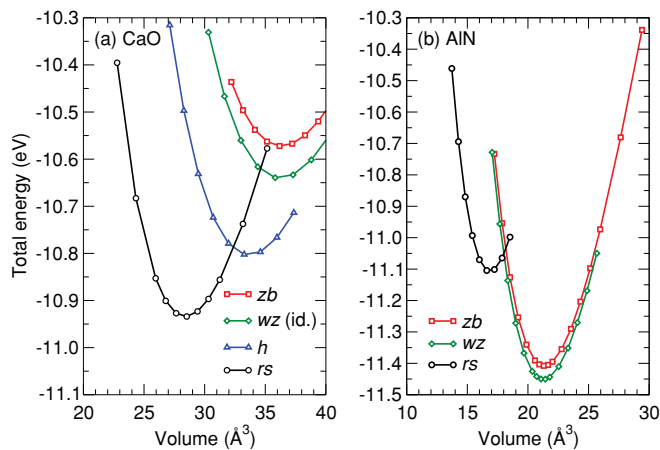
For detailed studies of bound states of band-edge excitons, we apply a recently developed scheme.[23] It is based on an iterative diagonalization to find the lowest eigenvalues of the excitonic Hamiltonian.

III. GEOMETRIES AND QUASIPARTICLE BAND STRUCTURES

A. Structural and energetic properties

The ground-state properties of CaO and AlN are studied for the B1 rs structure with space group $Fm\bar{3}m$ (O_h^5), the B3 zb structure with space group $F\bar{4}3m$ (T_d^2), and the B4 wz structure with space group $P6_3mc$ (C_{6v}^4). The energy-volume dependences are shown in Fig. 1. They clearly indicate that rs-CaO and wz-AlN are the equilibrium phases under ambient
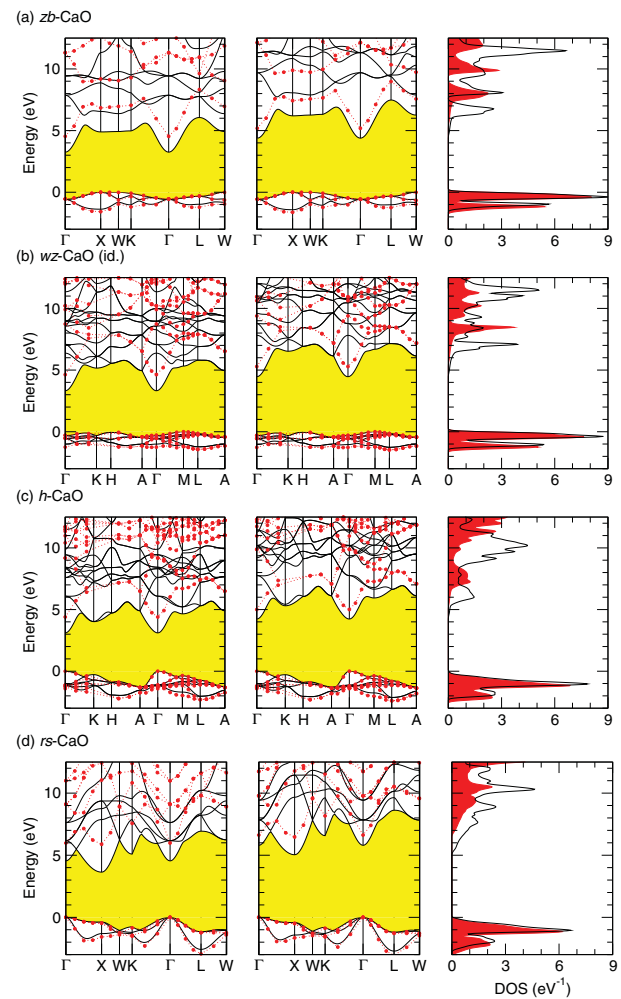

FIG. 2. (Color online) QP band structures and DOSs for (a) zb-, (b) id. wz-, (c) h-, and (d) rs-CaO calculated in different approaches. The starting electronic structure is given by solid lines (PBE in the left panels or HSE03 in the middle panels). The red circles denote the band energies with QP corrections. To guide the eye, the circles are connected by straight dotted lines. The yellow area indicates the fundamental gap region. The DOSs per formula unit in the right panels are given in the HSE03 (black solid lines) and HSE03+G_0W_0 (red shaded regions) approaches with a Lorentzian broadening of 0.2 eV. The VBM is used as energy zero.

FIG. 1. (Color online) Total energy versus volume per formula unit for various polymorphs of (a) CaO and (b) AlN.

TABLE I. Lattice parameters a (*fcc* crystal structures) or a, c, and u (hexagonal crystal structures) and cohesive energies E_{coh} for the CaO and AlN polymorphs. Experimental values are given in parentheses.

Parameter	CaO				AlN		
	zb	*wz* (id.)	*h*	*rs*	*zb*	*wz*	*rs*
a (Å)	5.257	3.714	4.015	4.844 (4.811[a])	4.404 (4.373[b])	3.131 (3.111[a])	4.071 (3.938[c])
c (Å)		6.065	4.822			5.020 (4.979[a])	
u		0.375	0.500			0.381	
E_{coh} (eV)	10.57	10.64	10.80	10.93 (11.0[d])	11.41	11.45 (11.52[e])	11.11

[a]From Ref. 35.
[b]From Ref. 48.
[c]From Ref. 49.
[d]From Ref. 50.
[e]From Ref. 51.

conditions (see also Ref. 35). If no additional constraints are applied in the case of CaO, an initial configuration in the ideal (id.) *wz* phase relaxes into the hexagonal B_k-BN structure with space group $P6_3/mmc$ (D_{6h}^4), which features an additional mirror plane. A similar behavior can be observed for MgO.[52,53] The B_k-BN crystal structure will be denoted as *h*-CaO in the following. In Fig. 1, results for both the ideal *wz* structure and *h*-CaO are given. The low-density phases *wz*-CaO and *zb*-CaO with fourfold coordination are significantly higher in energy compared with *h*-CaO. For AlN, the total energy of the *zb* structure is only 40 meV above the energy of the *wz* structure, whereas the *rs* structure represents a high-pressure phase in agreement with experimental findings.[49]

The structural parameters and cohesive energies are listed in Table I for all crystal structures. Because of the treatment of XC within the GGA, the lattice constants are overestimated by 0.6%–0.8% compared with available experimental results. The comparably large deviation in the case of *rs*-AlN may be due to the fact that it is more difficult to define the lattice parameters for a nonequilibrium high-pressure phase in experiment. The cohesive energies are in excellent agreement with measured values. Altogether, we state that the DFT-GGA geometries provide a reliable starting point for the computation of band structures and optical properties.

B. Band structures and densities of states

In Figs. 2 and 3, we show the band structures of CaO and AlN in several crystal structures calculated by means of the PBE and the HSE03 XC functionals with and without G_0W_0 QP corrections. In addition, the DOSs are depicted. For both materials, the sixfold coordinated *rs* structure gives rise to an indirect fundamental gap with the valence-band maximum (VBM) at the Γ point and the conduction-band minimum (CBM) at the X point of the BZ. In the *wz* geometries, both compounds are direct semiconductors with the fundamental gap located at Γ. For the *zb* crystals, however, an indirect gap appears close to the direct one with a somewhat smaller energy. The VBM in *zb*-CaO is located at the X point (within the PBE or HSE03 approach the energies of the highest valence band at the W and the X point are the same), while the CBM is still at Γ. For *zb*-AlN, the BZ location of the band extrema is just the reverse.

The gap values are listed in Table II. The PBE gaps are smaller than those obtained with the HSE03 functional, since the latter already includes important parts of the XC self-energy. The GW corrections mainly depend on the starting electronic structure. For the equilibrium polymorphs, the QP
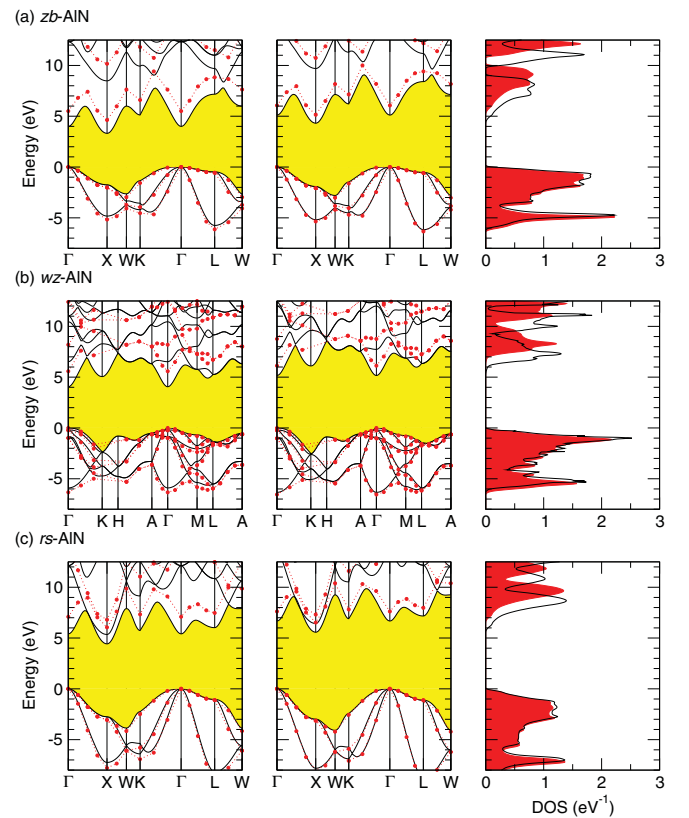

FIG. 3. (Color online) QP band structures and DOSs for (a) *zb*-, (b) *wz*-, and (c) *rs*-AlN calculated in different approaches. The starting electronic structure is given by solid lines (PBE in the left panels or HSE03 in the middle panels). The red circles denote the band energies with QP corrections. To guide the eye, the circles are connected by straight dotted lines. The yellow area indicates the fundamental gap region. The DOSs per formula unit in the right panels are given in the HSE03 (black solid lines) and HSE03+G_0W_0 (red shaded regions) approaches with a Lorentzian broadening of 0.2 eV. The VBM is used as energy zero.

TABLE II. Fundamental indirect and direct gaps (in eV) calculated within four different approaches. Experimental values are given for comparison.

	Gap	PBE	PBE+G_0W_0	HSE03	HSE03+G_0W_0	Exp.
zb-CaO	$X \rightarrow \Gamma$	3.25	4.53	4.39	5.19	
	$W \rightarrow \Gamma$	3.25	4.55	4.39	5.20	
	$\Gamma \rightarrow \Gamma$	3.83	5.08	4.96	5.75	
wz-CaO (id.)	$M \rightarrow \Gamma$	3.32	4.63	4.46	5.29	
	$\Gamma \rightarrow \Gamma$	3.64	4.93	4.78	5.59	
h-CaO	$\Gamma \rightarrow \Gamma$	3.11	4.40	4.23	5.00	
rs-CaO	$\Gamma \rightarrow X$	3.64	5.88	5.04	6.47	
	$\Gamma \rightarrow \Gamma$	4.54	5.98	5.80	6.63	7.09[a]
	$X \rightarrow X$	4.02	6.35	5.46	6.96	
zb-AlN	$\Gamma \rightarrow X$	3.32	4.62	4.32	5.15	5.34[b],5.3[c]
	$\Gamma \rightarrow \Gamma$	3.99	5.51	5.11	6.06	5.93[c]
wz-AlN	$\Gamma \rightarrow \Gamma$	4.05	5.58	5.16	6.13	6.11[d]
rs-AlN	$\Gamma \rightarrow X$	4.42	6.05	5.57	6.53	
	$\Gamma \rightarrow \Gamma$	5.41	7.09	6.67	7.62	

[a]From Ref. 54. Thermoreflectance measurements at 85 K.
[b]From Ref. 55. Ellipsometry measurements.
[c]From Ref. 56. Ellipsometry measurements at room temperature.
[d]From Ref. 57. Photoluminescence measured at 10 K.

shifts of the direct gaps at the Γ point amount to 1.4 eV (CaO) and 1.5 eV (AlN) starting from PBE eigenvalues or 0.8 eV (CaO) and 1.0 eV (AlN) on top of the HSE03 energies. These differences explain why the HSE03 starting point is more appropriate for a perturbational treatment of the QP equation (see also Ref. 44). Going along with the smaller gaps in the corresponding zeroth approximation, the PBE+G_0W_0 gaps prove to be smaller than the HSE03+G_0W_0 gap values. The HSE03+G_0W_0 gaps are much closer to the experimental results than the PBE+G_0W_0 values (see Table II) in agreement with the findings for many other semiconductors.[10,44,58]

The calculated direct gap of rs-CaO is slightly underestimated compared with measured values (see Table II). The deviation can partially be attributed to the use of PBE instead of experimental lattice constants. Yamasaki and Fujiwara[59] computed an indirect band gap of 3.65 eV in the local-density approximation (LDA) which proves to be very close to our PBE result. However, they obtained a Γ-X gap of 6.64 eV in LDA+G_0W_0 which is well above our PBE+G_0W_0 gap of 5.88 eV and even above our HSE03+G_0W_0 gap of 6.47 eV. The reason may be the coarse **k**-point sampling used in Ref. 59.

For zb-AlN, an indirect band gap of 5.34 eV[55] or 5.3 eV[56] is deduced from the weak onset of the optical absorption in ellipsometry experiments. Our calculated value of 5.15 eV for the Γ-X gap is only somewhat smaller. The deviation might be due to the use of the PBE lattice constant which is slightly larger than the experimental value (see Table I). Thus, the calculated band gap can be expected to underestimate the true fundamental gap slightly. Further, Röppischer et al.[56] state that their value should be considered as an upper limit for the indirect band gap. The computed direct gaps for zb- and wz-AlN are in excellent agreement with recent experimental data derived from ellipsometry measurements[56] or photoluminescence spectra.[57]

LDA+G_0W_0 calculations predict an indirect band gap of 4.9 eV (Ref. 60) or 5.45 eV (Ref. 25) and a direct gap of 6.0 eV (Ref. 60) or 6.72 eV (Ref. 25) for zb-AlN. The gap of wz-AlN is stated to be 5.8 eV (Ref. 60) or 6.8 eV (Ref. 25). Both Rubio et al.[60] and Bechstedt et al.[25] use model approaches to describe the wave-vector and frequency dependence of the dielectric function to reduce the computational work load. Deviations in the resulting gaps are most probably due to differences in the details of the implementation and the usage of experimental lattice constants and norm-conserving pseudopotentials[60] or LDA lattice parameters and ultrasoft pseudopotentials.[25] However, in the calculations presented here, the full wave-vector and frequency dependence of the dielectric matrix are taken into account.[45] In the same spirit as the present work, Rinke et al.[61] used an improved starting point, in their case the exact-exchange optimized-effective-potential method with LDA correlation, for the G_0W_0 calculation. They obtained 5.63 eV (indirect gap of zb-AlN), 6.53 eV (direct gap of zb-AlN), and 6.47 eV (direct gap of wz-AlN) and, hence, a slight overestimation of the experimental findings (see Table II). In the light of both the recent theoretical and experimental results, it can be concluded that the so-called recommended value of 4.9 eV[62] for the indirect gap of zb-AlN has to be revised.

IV. OPTICAL ABSORPTION SPECTRA, CRITICAL POINTS, AND EXCITONS

In this section, we discuss the optical absorption spectra with and without excitonic effects for the polymorphs rs-CaO (Fig. 4), zb-AlN (Fig. 6), and wz-AlN (Fig. 9) that have been grown up to now. The spectra clearly show the most important influences of the excitonic effects on the optical absorption: (i) There is a clear tendency for a redistribution of oscillator strength from higher to lower photon energies due to the Coulomb attraction. (ii) Bound excitonic states, i.e.,

pair excitations with finite binding energies, at the absorption edge (see Fig. 9) or even within the interband continuum (see Fig. 4), can occur.

Aiming for a critical-point analysis of optical absorption spectra, one has to keep in mind that the JDOS is not necessarily large at a critical point. For instance, the JDOS is zero at the M_0 point, which marks the absorption onset and rises proportionally to the square root of the energy for parabolic bands thereafter. Consequently, no distinct peaks that can be identified with van Hove singularities are visible in absorption spectra calculated within the IPA or IQPA, which are merely JDOSs multiplied with the optical transition matrix elements. Only the inclusion of excitonic effects in the calculation may lead to pronounced peaks near critical-point energies. The bound excitonic states with large oscillator strengths which are located in the vicinity of M_0 points (Ref. 63) and the line-shape modifications at M_1 points (Refs. 64 and 65) act as a kind of marker which allows us to identify the approximate energetic position of the critical point. However, the excitonic peaks are shifted by their binding energy with respect to the energy of the corresponding van Hove singularity. The identification of M_2 and M_3 points in the spectra is by far more difficult. In these cases, the inclusion of the attractive Coulomb interaction leads to a reduction of spectral strength and smears out structures in the JDOS.[64]

A. *rs*-CaO

In Fig. 4 the absorption spectra of rs-CaO are shown both with and without local-field and excitonic effects. We find qualitative agreement of the overall line shape between our calculation in the IQPA, where the HSE03+G_0W_0 eigenvalues have been employed, and an IPA spectrum[67] using DFT-LDA. The main difference results from the neglect of QP corrections in Ref. 67, which lead to a nearly rigid blueshift of roughly 3 eV. However, Fig. 4 shows that the inclusion of excitonic effects is essential.
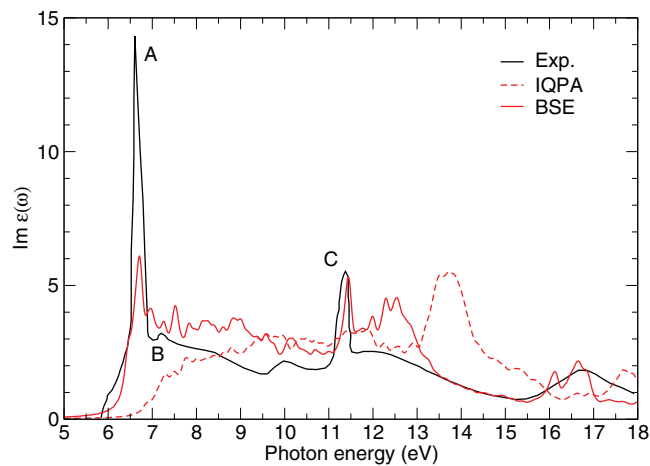
The experimental absorption spectrum of rs-CaO[66] (Fig. 4) shows three distinct peaks, A, B, and C, at photon energies of $\hbar\omega = 6.8$, 7.1, and 11.4 eV. Additional broad features appear at about $\hbar\omega = 10.0$ and 16.9 eV. The calculated spectrum with excitonic effects possesses a similar line shape. The theoretical peak positions at $\hbar\omega = 6.71$ and 11.44 eV agree very well with the experimentally observed positions of the A and C peaks. The same holds for the broad features near $\hbar\omega = 10.1$, 12.5, and 16.6 eV. Only the B peak cannot be identified unambiguously. The structure near 12.5 eV forms a shoulder in the experimental spectrum. Also the absolute values of the imaginary part of the dielectric function agree well, in particular taking into consideration that they are comparably small.

Whited and Walker[66] identify the three most distinct absorption peaks A, B, and C with excitons. The A peak at 6.71 eV is not below the direct QP gap of 6.63 eV at Γ, and, hence cannot be a band-edge exciton. Phonon-assisted transitions related to the indirect gap at 6.47 eV do not play a role, since the theoretical approach presented here is restricted to vertical optical transitions. A refined analysis of the A peak is given in Sec. V A, where it is shown that it belongs to a Wannier–Mott-like exciton originating mainly from the lowest-energy transition at the X point, which is a M_0 critical point (see Fig. 5). The strength of peak A seems to be somewhat underestimated. The reason for this is that the height of isolated peaks in the computed spectra strongly depends on the applied lifetime broadening. For the spectrum shown in Fig. 4, a broadening of $\eta = 0.1$ eV has been used for all spectral regions. Even smaller lifetime broadenings would require a denser **k**-point sampling, especially for spectral regions with a plateau-like line shape. The resolution of the experimental reflectance data ranges from 3.5 meV at low energies to 250 meV at high energies.[66] Therefore, the A peak proves to be sharper in the measured spectrum. In addition, the experimental curve has been extracted from reflectance spectra using a Kramers–Kronig inversion, which introduces
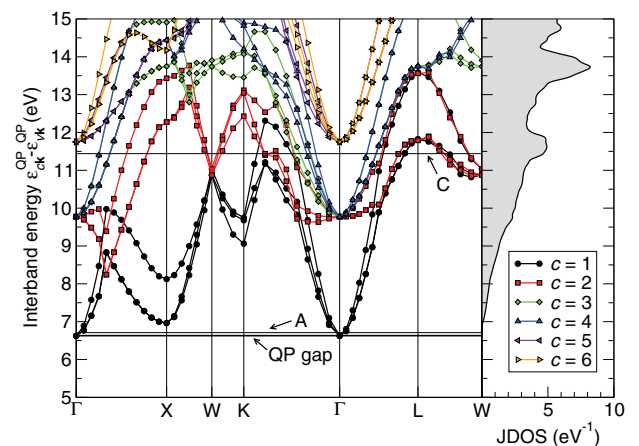

FIG. 4. (Color online) Imaginary part of the dielectric function of rs-CaO. The spectrum in the IQPA (red dashed line) and the solution of the BSE including excitonic and local-field effects (red solid line) are shown. Experimental data from Ref. 66 (black solid line) are given for comparison. A Lorentzian broadening of $\eta = 0.1$ eV has been used for the calculated curves.

FIG. 5. (Color online) Joint band structure and JDOS for rs-CaO in the HSE03+G_0W_0 approach. The interband-transition energies from all valence bands v to the lowest conduction bands $c = 1, \ldots, 6$ are shown. The calculated positions for the QP gap and the A and the C excitons are indicated.

TABLE III. Optical transition energies E_i, E_i', and E_i'' (in eV) from the highest valence to the first three conduction bands at the high-symmetry points of the *fcc* BZ for *rs*-CaO. The energies are taken from HSE03+G_0W_0 calculations (see Fig. 2).

Point	Label i	E_i	E_i'	E_i''
Γ	0	6.63	9.77	11.75
L	1	11.79	11.82	13.75
X	2	6.96	12.27	13.75
W	3	10.87	13.74	15.28
K	4	9.06	12.43	13.45

significant errors at the low- and high-frequency end points of the data.[66]

In our calculated curves, the faint peak *B* cannot be resolved. This may be an issue of **k**-point convergence. The weakly varying amplitude of the absorption spectrum above the *A* peak asks for a finer **k**-point sampling. On the other hand, the JDOS (see Fig. 5) does not exhibit any critical points in the relevant energy range. Experiments[68] relate the weak feature *B* to the Γ-point exciton based on the occurrence of spin-orbit and exciton-phonon split-off peaks. However, Table III shows that the direct gap at the BZ center is smaller than the one at the *X* point, which renders this interpretation implausible in the light of the calculations performed within this paper. But the *X* and the Γ gap are so close in energy that an interchange of the energetic positions due to strain in the sample may be possible.

To investigate the origin of the *C* peak, the joint band structure, i.e., the interband-energy differences $\varepsilon_{c\mathbf{k}}^{\text{QP}} - \varepsilon_{v\mathbf{k}}^{\text{QP}}$ (in analogy to the JDOS), is plotted in Fig. 5 to simplify the identification of critical points. Whited and Walker[66] support the hypothesis that the *C* exciton stems from transitions between the third-highest valence band and the lowest conduction band at the *X* point. Based on the QP band structures calculated here (see Fig. 2), this view cannot be confirmed: The corresponding transition energy of 8.12 eV (see Fig. 5) is too small. Taking into account a finite binding energy for the exciton, the transitions E_0'' (at the Γ point) and E_1/E_1' (at the *L* point) come into question (see Fig. 5 and Table III). On the other hand, E_1 and E_1' are M_3 critical points, and, thus, no excitonic peaks should occur.[29] This renders E_0'' the only remaining alternative. The argumentation can be strengthened by the observation that E_0'' is a M_0 critical point with large oscillator strength.

Moreover, Fig. 5 suggests that the broad feature around 10 eV might be traced back to transitions from the threefold degenerate VBM at Γ to the threefold degenerate second conduction band. The corresponding "joint bands" are comparably flat over wide areas of the BZ, but do not lead to a strong peak in the JDOS. The dominant feature below 14 eV in the IQPA spectrum is also an accumulation of many interband transitions with different origins in the BZ but high JDOSs (see Fig. 5).

B. *zb*-AlN

Figure 6 shows the imaginary part of the dielectric function for *zb*-AlN in the IQPA as well as the dielectric function including excitonic effects. First, one observes a tremen-
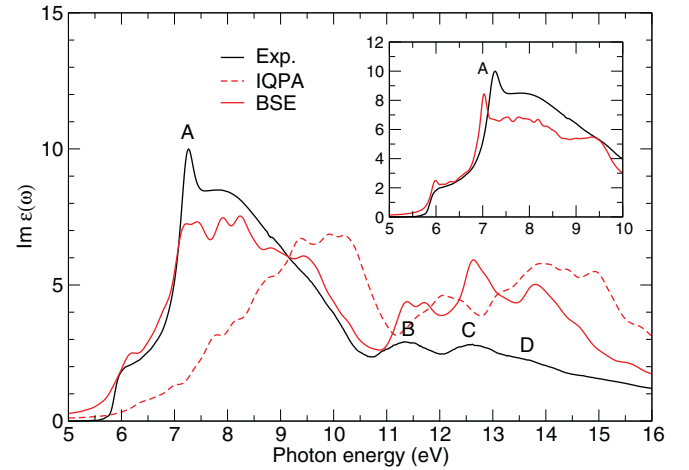

FIG. 6. (Color online) Imaginary part of the dielectric function of *zb*-AlN. The spectrum in the IQPA (red dashed line) and the solution of the BSE including excitonic and local-field effects (red solid line) have been calculated using an $18 \times 18 \times 18$ **k**-point mesh, a cutoff of 20 eV, and a Lorentzian broadening of $\eta = 0.2$ eV. Experimental data from Ref. 56 (black solid line) are given for comparison. For the inset, the low-energy range of the spectrum has been computed with a refined resolution employing a $40 \times 40 \times 40$ mesh, a cutoff of 10 eV, and a broadening of $\eta = 0.1$ eV. Due to the increased number of **k** points, a scissors shift instead of G_0W_0 QP corrections had to be employed in this case.

dous redistribution of spectral strength to lower energies, emphasizing the importance of including the electron-hole interaction. The onset of the spectrum is characterized by a steep rise in the optical absorption. With a moderate **k**-point sampling of $18 \times 18 \times 18$ mesh points and a broadening of $\eta = 0.2$ eV, the solution of the BSE exhibits a plateau-like region between 7 and 9.5 eV (see Fig. 6), which converges very slowly with increasing **k**-point sampling. However, the peak *A*, which is visible in the most recent high-resolution spectral ellipsometry measurements[56] at 7.26 eV is absent in the computed curve and the oscillator strength of the plateau seems to be underestimated. At higher energies, broad peaks, labeled *B*, *C*, and *D*, are found in the calculated spectrum in the vicinity of $\hbar\omega = 11.5$, 12.6, or 13.8 eV, respectively. The positions of peaks *B* and *C* agree reasonably well with experimental absorption maxima at 11.14 and 12.52 eV. However, the spectral strength differs remarkably. Possible reasons may be the sample quality or corrections used in the extraction of the dielectric function from the ellipsometry data.

Previous *ab initio* studies[25,69] comprise only the low-energy range of the spectrum and agree very well with the results shown here except for slight differences in the peak positions and intensities, which are due to the improved calculation of QP energies and optical transition matrix elements in the present work (see Sec. II). References 25 and 69 likewise observe the plateau-like behavior of Im $\varepsilon(\omega)$ between 7 and 9.5 eV, since the number of **k** points employed there is comparable to the one used to calculate the spectrum in Fig. 6.

To resolve the fine structure of the absorption spectrum in the low-energy range, an increased BZ sampling with $40 \times 40 \times 40$ **k** points is applied (see inset of Fig. 6). Thereby, the BSE cutoff has to be reduced to 10 eV to keep the size

of the Hamiltonian computationally tractable. Further, it is prohibitive to calculate G_0W_0 QP corrections for such a large number of **k** points. For that reason, a scissors operator of $\Delta^{QP} = 0.95$ eV, which ensures the reproduction of the direct HSE03+G_0W_0 QP gap, has been used. The price to pay is slightly redshifted high-energy interband transitions due to the neglect of the frequency dependence of the QP shifts. With the refined **k**-point sampling we obtain good agreement between theory and experiment: The experimentally observed *A* peak at 7.26 eV (Ref. 56) becomes clearly visible. (The deviating value of $\hbar\omega = 7.204$ eV given in the text of Ref. 56 is a result of the assumed deconvolution of the measured spectrum.) Its height above the plateau fits very well.

In the following we want to point out to what extent it is possible to assign critical-point energies to characteristic features in the absorption spectrum of *zb*-AlN. To this end, the joint band structure and JDOS of *zb*-AlN are plotted in Fig. 7. Further, the QP transition energies at high-symmetry points are given in Table IV. In contrast to most diamond-structure or zinc-blende semiconductors, such as Si, Ge, or GaAs, whose critical points follow the energetic sequence E_0, E_1, E_0', E_2, E_1' (see Ref. 29), one observes the ordering E_0, E_2, E_1, E_1', E_2', E_0' for *zb*-AlN (see Table IV). Especially, the interchange of E_1 and E_2 and the extremely high-lying E_0' transition render the interpretation of the experimental absorption spectrum difficult. The reversed ordering of the E_1 and E_2 critical points has been discussed recently by Röppischer *et al.*[56] However, their identification of peak positions matches only for E_2 at 7.2 eV (using the denotation of the present paper; labeled E_1 in Ref. 56) with the calculated QP transition energies, whereas the peaks denoted as E_1 at 7.95 eV, E_1' at 11.14 eV, and E_0' at 12.52 eV are in obvious disagreement with the values listed in Table IV. This suggests that the interpretation of spectra of nitrides and oxides is more difficult and cannot be based solely on chemical trends derived for compounds without first-row anions. The only obvious tendency is the increasing energy of the E_0' transition due to the increasing energetic difference of

the atomic *p* valence levels of the constituents when going to lighter anions in the series of III-V compounds.[51]

The pronounced *A* peak in Im $\varepsilon(\omega)$ (see Fig. 6) can be unambiguously assigned to an M_0 critical point which stems from the transitions between the highest valence and lowest conduction band at the *X* point of the BZ (see Fig. 7). The plateau between 7 and 9.5 eV, by contrast, cannot be identified with a single critical point. Figure 7 shows that, even though the M_1 critical point at the *L* point lies only slightly above the energy range in question, transitions from the three highest valence bands into the lowest conduction band contribute to the optical absorption over large parts of the BZ and form the plateau.

The same holds for the broad feature *B* in Fig. 6. There are many transitions from the second- and third-highest valence bands to the lowest conduction band in the relevant energy range, thus prohibiting a unique identification of the peak with a single critical point. However, the *B* peak is clearly not associated with the E_1' transition, which occurs at higher photon energies. Also the considerable width of the feature *B* and its double-peak structure in the calculations (see Fig. 6) suggest that it does not originate from a single critical point.

Peak *C* in Fig. 6, on the other hand, shows clear excitonic modifications, in particular enhancement of oscillator strength, when the electron-hole interaction is included in the calculations. This observation indicates that it may be due to critical points and not to an overall high JDOS in this energy range. The joint band structure in Fig. 7 reveals that the M_0 critical point E_2' and the M_2 critical point E_1' lie slightly above the *C* peak. The latter, however, cannot not be responsible for the enhancement of oscillator strength, since M_2 critical points rather cause a damping,[64] thus leaving E_2' as the only remaining alternative. Therefore, we can clearly contradict the assignment of the *C* peak to the E_0' critical point by Röppischer *et al.*[56]

The *D* peak, which is merely a very faint feature in the experimental spectrum (see Fig. 6), can be associated with the M_0 critical point E_1'' (see Fig. 7 and Table IV). However, once more there are many bands contributing to the peak over large parts of the BZ, as becomes obvious from Fig. 7.

To strengthen our argumentation, Fig. 8 attempts to visualize the contributions of different **k**-space regions to the imaginary part of the dielectric function including excitonic effects. For this purpose, the full BSE spectrum, comprising all **k** points in the BZ, as well as spectra excluding spherical regions with radii of $0.05 \times 2\pi/\text{Å}$ ($0.1 \times 2\pi/\text{Å}$) around the high-symmetry points Γ, *X*, and *L* are shown. That means that

TABLE IV. Optical transition energies E_i, E_i', and E_i'' (in eV) from the highest valence to the first three conduction bands at the high-symmetry points of the *fcc* BZ for *zb*-AlN. The energies are taken from HSE03+G_0W_0 calculations (see Fig. 3).

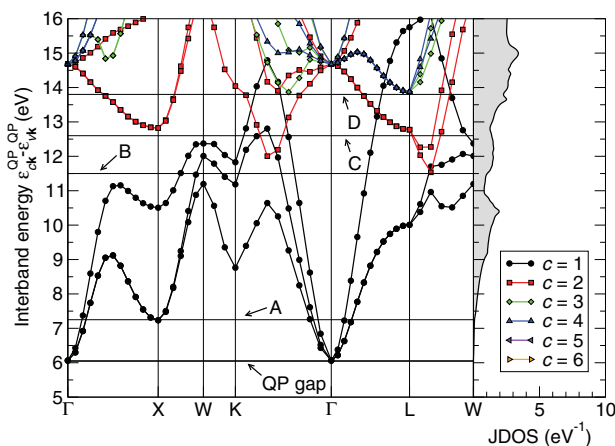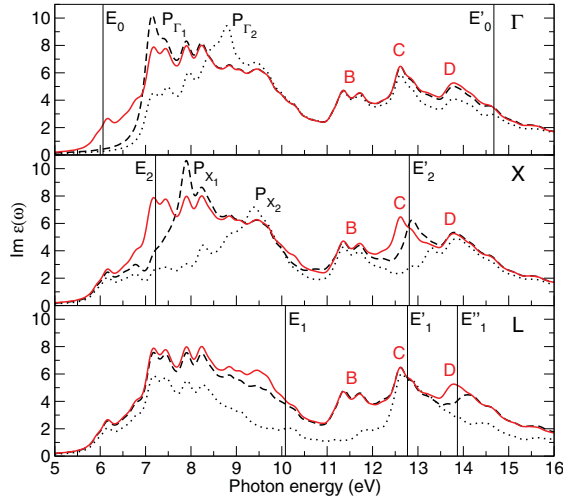| Point	Label i	E_i	E_i'	E_i''
Γ	0	6.06	14.67	20.31
L	1	10.00	12.77	13.88
X	2	7.22	12.81	18.66
W	3	11.20	16.80	17.03
K	4	8.76	14.04	17.29

FIG. 7. (Color online) Joint band structure and JDOS for *zb*-AlN in the HSE03+G_0W_0 approach. The interband-transition energies from all valence bands *v* to the lowest conduction bands $c = 1, \ldots, 6$ are shown. The calculated positions for the QP gap and the *A*, *B*, *C*, and *D* peaks are indicated.

FIG. 8. (Color online) Contributions of different **k**-space regions to the optical absorption of zb-AlN. The red solid line depicts the solution of the BSE for the entire BZ. Further, spectra omitting spheres with radii of $0.05 \times 2\pi \text{Å}^{-1}$ (black dashed line) or $0.1 \times 2\pi \text{Å}^{-1}$ (black dotted line) in **k** space around the high-symmetry points Γ, X, and L are shown. The transition energies of important critical points are indicated. A Lorentzian broadening of $\eta = 0.15$ eV has been applied in the calculations.

contributions of 1% (9%) for Γ, 3% (27%) for X, or 4% (36%) for L of the BZ volume are left out. Consequently, one would expect a reduction of the oscillator strength of a peak in the spectrum if this peak mainly stems from a critical point whose vicinity in **k** space has been excluded from the calculations. However, there are two counteracting effects: First, there are additional line-shape modifications due to the neglect of the interaction between the excluded transitions and the remaining ones. Second, an enhancement of oscillator strength near the energy of the excluded critical point can also occur. The neglect of optical transitions near M_0 critical points simulates a Pauli blocking, as is known, for instance, from the occurrence of degenerate electron gases in conduction-band valleys of doped semiconductors, which should be accompanied by the formation of a Fermi-edge singularity as in the case of Mahan excitons.[70,71] In contrast to Mahan excitons, where also the screening of the electron-hole interaction is modified, an artificial enhancement of the oscillator strength at the singularity can be found.

If the surrounding of the Γ point is excluded from the calculation of the spectrum, indeed the contributions to the E_0 structure disappear. For E_0', this effect is significantly weakened due to the comparably strong contributions of other transitions in the relevant spectral region. Similarly pronounced reductions occur near the E_2 (A peak) and the E_2' (C peak) critical-point energies if the vicinity of the X points is omitted, thus indicating strong contributions of optical transitions around the X points to these spectral features, in agreement with the analysis of the joint band structure. Further, it can be shown that the exclusion of the L points leads to a reduction of the E_1' structure (D peak). However, the C peak near E_1' remains uninfluenced, suggesting that the contribution of optical transitions near the L points is negligible for the reasons discussed above. In the low-energy
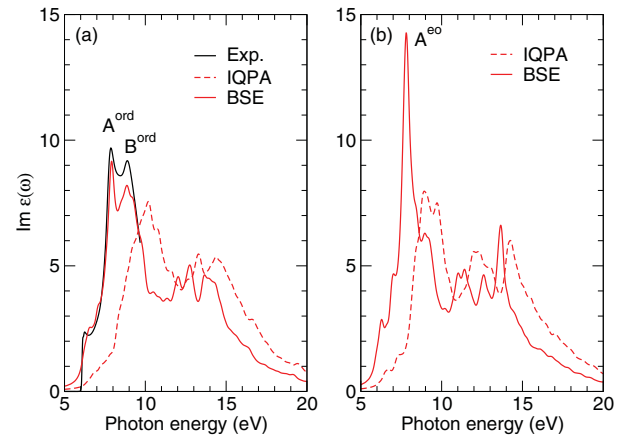

FIG. 9. (Color online) Imaginary part of the dielectric function of wz-AlN for (a) ordinary and (b) extraordinary polarization. The spectrum in the IQPA (red dashed line) and the solution of the BSE including excitonic and local-field effects (red solid line) are depicted. Experimental data from Ref. 72 (black solid line) are given for comparison. A Lorentzian broadening of $\eta = 0.2$ eV has been applied.

range, one observes the artificial peaks P_{Γ_1} (P_{Γ_2}) or P_{X_1} (P_{X_2}), stemming from the Coulomb enhancement effects due to the Pauli blocking. As stated before, such a behavior is characteristic for the exclusion of spherical **k**-space regions around M_0 critical points and renders this kind of analysis so difficult.

C. wz-AlN

In Fig. 9, the computed absorption spectra of wz-AlN are shown for ordinary (ord.) and extraordinary (eo.) light polarization. Apart from the bound excitonic state at the absorption onset, which will be discussed in detail in Sec. V C, the low-energy range of Im $\varepsilon(\omega)$ is governed by a double-peak structure, labeled A^{ord} and B^{ord}, at photon energies of $\hbar\omega = 7.9$ and 8.9 eV for ordinary polarization. The extraordinary polarization direction exhibits a peak denoted as A^{eo} at $\hbar\omega = 7.8$ eV and a shoulder around 9.0 eV. In the high-energy range, we find peaks at $\hbar\omega = 12.0$ and 12.7 eV as well as a pronounced structure around 14 eV in the ordinary polarization direction. For extraordinary polarization, a three-peak structure located around 11.2, 12.6, and 13.7 eV occurs.

We observe good agreement with previous computations:[25,73] This holds particularly for the peak positions. In comparison with Ref. 73 even the peak intensities agree. Because of the use of PAW wave functions and the ameliorated treatment of the optical transition matrix elements in the present paper, we find higher oscillator strengths compared with the spectra presented in Ref. 25.

The experimental absorption spectrum of wz-AlN,[72] which is known only up to photon energies of 9.8 eV, is in very good agreement with the solution of the BSE (see Fig. 9). The matching of the peak positions is excellent, and also the deviations in the peak intensities are smaller than 10%.

To analyze the absorption spectra in terms of critical points, the joint band structure and JDOS as well as the QP transition energies are given in Fig. 10 and Table V, respectively. They were obtained using a $12 \times 12 \times 10$ **k**-point mesh, since the
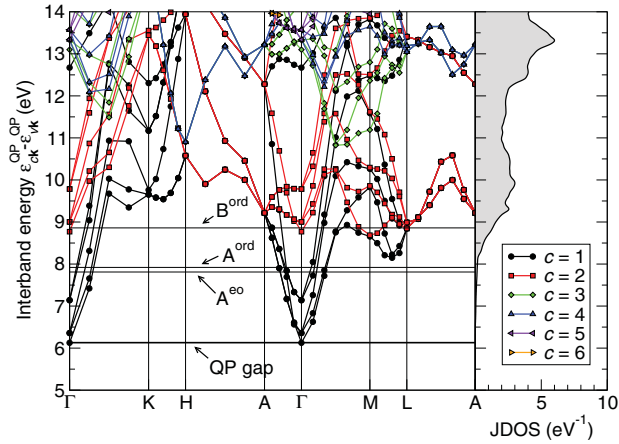
FIG. 10. (Color online) Joint band structure and JDOS (per formula unit) for wz-AlN in the HSE03+G_0W_0 approach. The interband-transition energies from all valence bands v to the lowest conduction bands $c = 1, \ldots, 6$ are shown. The calculated positions for the QP gap, the A^{ord} and B^{ord} peaks in ordinary light polarization, and the A^{eo} peak in extraordinary polarization are indicated.

$8 \times 8 \times 6$ grid does not comprise all high-symmetry points of the BZ. The excitonic peak at the absorption onset can be unambiguously assigned to the E_0 transition at the Γ point. The peaks A^{ord} and A^{eo}, which are very close in energy, are clearly due to the M_0 critical point at 8.15 eV along the M-L line. Due to the strong electron-hole interaction, the excitonic peak is redshifted by about 0.3 eV compared with the QP transition energy in the joint band structure (see Fig. 10). Furthermore, this bound excitonic state is in resonance with the continuum of single-particle transitions.

In contrast to the A peaks, the B peak in ordinary polarization or the shoulder in extraordinary polarization cannot be identified with a single critical point in the JDOS of wz-AlN. Interband transitions from large parts of the BZ contribute to the optical absorption in the relevant energy range (see Fig. 10). For instance, the points E_0', E_1, E_2, and E_2' match approximately in terms of their transition energies, but this holds also for interband transitions apart from the high-symmetry points. As is obvious from Fig. 10, such a critical-point analysis becomes impossible for the absorption peaks above 10 eV. In our opinion, an assignment of the peaks to certain interband transitions just by looking on a band structure derived within the empirical pseudopotential method[74] is highly doubtful.

TABLE V. Optical transition energies E_i, E_i', and E_i'' (in eV) at the high-symmetry points of the hexagonal BZ for wz-AlN. The energies are taken from HSE03+G_0W_0 calculations (see Fig. 3).

Point	Label i	E_i	E_i'	E_i''
Γ	0	6.13	8.77	13.10
L	1	8.85	13.05	15.94
M	2	8.66	8.70	11.20
A	3	9.22	13.22	14.31
K	4	9.65	13.44	14.84
H	5	10.58	10.90	15.55

V. NEAR-BAND-EDGE EXCITONS

The discussion of the spectral features in Sec. IV was based on the computation of the dielectric function $\varepsilon(\omega)$ in a wide range of photon energies. Here, we focus on the absorption edge. The pair-excitation energies E_Λ, i.e., the solutions of the eigenvalue problem in Eq. (1), and the corresponding oscillator strengths,

$$f_\Lambda(\hat{\mathbf{q}}) = \frac{2\,m_0}{\hbar^2} \left| \sum_{cv\mathbf{k}} M_{\hat{\mathbf{q}}}(cv\mathbf{k})\, A_\Lambda^*(cv\mathbf{k}) \right|^2 E_\Lambda, \qquad (5)$$

of the lowest pair excitations are calculated as described in Ref. 23 in detail.

In principle, excitonic binding energies can be derived from the difference between the QP gap and the pair-excitation energies of the bound excitonic states. However, such binding energies have to be handled with due care. For the description of Wannier–Mott-like excitons that occur in materials with parabolic band extrema, extremely high $\mathbf{k}$-point densities are necessary (see discussion on convergence in Ref. 23). In the approach presented here, i.e., using HSE03+G_0W_0 QP energies, such dense $\mathbf{k}$-point samplings cannot be achieved (see Sec. II). That is why we are restricted to qualitative answers concerning exciton binding energies and oscillator strengths. The experience gained for the Wannier–Mott model, MgO, and InN[23] suggests that an increased BZ sampling would lead to larger binding energies. On the other hand, there is a partial error cancellation between too coarse $\mathbf{k}$-point samplings and the neglect of the lattice contributions to the screening of the Coulomb interaction. Taking the latter into account leads to larger dielectric constants and, hence, reduced binding energies of Wannier–Mott-like excitons if the longitudinal optical phonon frequencies are larger than the exciton binding energies.[25,75]

However, in the present paper, the focus lies on another issue. We primarily intend to unravel the location of the excitons in the BZ to answer the questions related to their identification with critical points. For this purpose, the applied $\mathbf{k}$-point sets are sufficient. To visualize the $\mathbf{k}$-space distribution of bound excitonic states, the quantity

$$C_\Lambda(\mathbf{k}) = \sum_{cv} |A_\Lambda(cv\mathbf{k})|^2, \qquad (6)$$

which can be regarded as a density distribution of the exciton in reciprocal space, is analyzed.

A. rs-CaO

The pair-excitation energies in the vicinity of the absorption edge of CaO as well as the corresponding oscillator strengths are shown in the upper panel of Fig. 11. One finds two threefold degenerate eigenvalues, labeled E_{Γ_1} and E_{Γ_2}, 171 and 21 meV below the QP gap (see Fig. 11), which correspond to the critical point E_0 and stem from transitions near the threefold degenerate VBM Γ_{15v} and the CBM Γ_{1c}. These excitations constitute the lowest bound excitonic states, i.e., the 1s and 2s levels, of a Wannier–Mott-like exciton series. However, the typical $1/n^2$ behavior for the binding energies or $1/n^3$ behavior for the oscillator strengths, with n running over positive integers, cannot be observed due to the inclusion of the
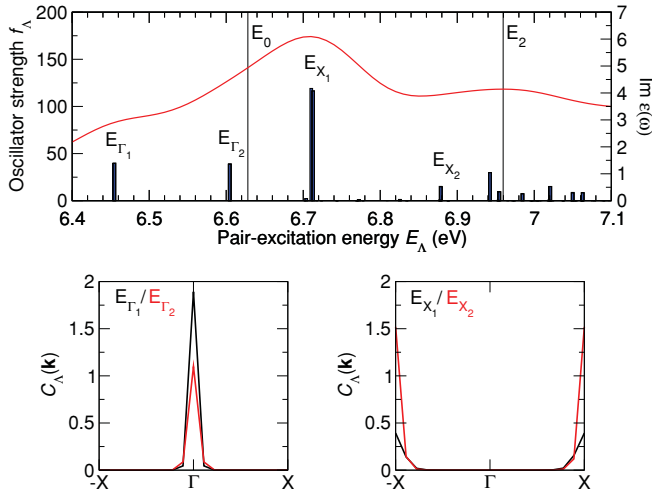
FIG. 11. (Color online) Pair-excitation energies E_Λ and oscillator strengths f_Λ of CaO near the absorption edge. For comparison, the imaginary part of the dielectric function with $\eta = 0.1$ eV is indicated by the red solid line (upper panel). The lower panels visualize the distribution of the excitonic wave function in reciprocal space for selected pair excitations marked in the upper panel.

full (nonparabolic) band structure as well as the convergence issues discussed above. In the lower panel of Fig. 11, the localization of the excitonic wave function in **k** space is shown for the states E_{Γ_1} and E_{Γ_2}, which clearly reveals the strong contributions from the BZ center.

Above the fundamental gap, six nearly degenerate eigenvalues denoted as E_{X_1} occur. They are followed by another group of sixfold degenerate eigenvalues labeled E_{X_2}. The plot of the corresponding excitonic wave functions in reciprocal space (see Fig. 11) shows that these excitations are almost completely due to transitions near the X points of the BZ. They constitute bound excitonic states with respect to the M_0 critical point E_2 ($X_{5'v} \rightarrow X_{3c}$) and have binding energies of 254 and 84 meV within the reached level of convergence. This is in excellent agreement with the assignment of the A peak in the absorption spectrum to the E_2 critical point (see Sec. IV A). In principle, Fano resonances[76] can occur if the bound states of higher critical points are interacting with the underlying continuum of interband transitions. However, a much denser **k**-point sampling would be necessary to resolve such a fine structure in the absorption spectrum. The sixfold degeneracies of the E_{X_1} and E_{X_2} excitations originate from the twofold degenerate valence-band state $X_{5'v}$ (see Fig. 2) and the occurrence of three equivalent X points in the fcc BZ.

B. zb-AlN

The situation in zb-AlN is quite comparable to the one observed for CaO because of the common cubic symmetry in the absence of spin-orbit coupling. We also find a threefold degenerate eigenvalue labeled E_{Γ_1}, which lies 122 meV below the absorption edge. Its excitonic wave function is localized in the surroundings of the Γ point. However, the second triplet E_{Γ_2}, which originates from the vicinity of the BZ center as well, lies above the E_0 critical point energy and is, therefore, not a bound excitonic state. As shown in Ref. 23
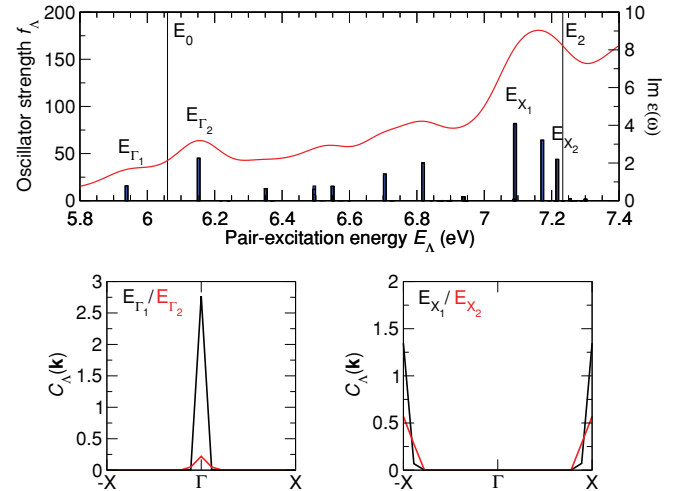

FIG. 12. (Color online) Pair-excitation energies E_Λ and oscillator strengths f_Λ of zb-AlN near the absorption edge. The imaginary part of the dielectric function with $\eta = 0.1$ eV is indicated by the red solid line (upper panel). The lower panels visualize the distribution of the excitonic wave function in reciprocal space for selected pair excitations marked in the upper panel.

such a behavior may be a consequence of a too coarse **k**-point sampling.

In accordance with the analysis in Sec. IV B, one finds bound excitonic states which are associated with the E_2 critical point. The sixfold degenerate eigenvalues E_{X_1} and E_{X_2} with binding energies of 143 and 19 meV can be clearly attributed to the X points of the BZ (see Fig. 12).

C. wz-AlN

In wz-AlN, the crystal-field splitting between the Γ_5 and Γ_1 states amounts to -235 meV in the HSE03+G_0W_0 approach. This value is close to measured splittings of -230 meV (Ref. 77) and -225 meV (Ref. 78). The crystal field is responsible for a significant polarization anisotropy of the optical absorption edge. In Fig. 13, excitation energies and oscillator strengths of the lowest pair excitations in ordinary and extraordinary polarization directions are given. Because of the negative sign of the crystal-field splitting the absorption edge associated with the QP transition $\Gamma_{1v} \rightarrow \Gamma_{1c}$ in extraordinary polarization occurs below the absorption edge in the ordinary polarization direction, which is related to the $\Gamma_{5v} \rightarrow \Gamma_{1c}$ transition. The bound excitonic states with respect to the particular absorption edges are denoted as A or B/C (see Fig. 13). Their absolute positions at 5.99, 6.22, and 6.22 eV agree well with the experimentally found peak positions at 6.025, 6.243, and 6.257 eV (Ref. 77) or 6.029, 6.243, and 6.268 eV (Ref. 78). This reasonable agreement of the absolute values and their splittings is really surprising taking into account that spin-orbit interaction and lattice screening effects have been neglected in the theoretical description and strain in the samples might bias the experimental results. However, the exciton binding energies of 138 meV (A) and 148 meV (B/C) are too large compared with the most recent experimental results of 58 meV from ellipsometry measurements.[79] Model calculations[80] using an anisotropic Wannier–Mott ansatz with
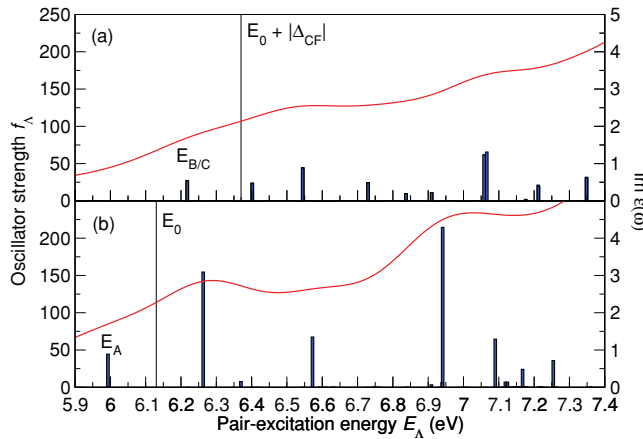
FIG. 13. (Color online) Pair-excitation energies E_Λ and oscillator strengths f_Λ near the absorption edge of wz-AlN for (a) ordinary and (b) extraordinary polarization. The imaginary part of the dielectric function with $\eta = 0.2$ eV is indicated by the red solid line.

effective dielectric constants yield binding energies of 51 meV. An *ab initio* method, which includes the lattice screening effects properly and may resolve the discrepancies, is yet to be developed.

VI. SUMMARY AND CONCLUSIONS

In the present paper, we have calculated the QP band structures of CaO and AlN in the rs, zb, and wz structures. Thereby, the QP equation in the G_0W_0 approximation has been solved perturbatively on top of the self-consistent solution of a QP equation in which the self-energy is described by the nonlocal HSE03 hybrid functional. Accurate values for the indirect and direct band gaps of all polymorphs have been derived, which are in excellent agreement with the available experimental results. Significant improvements over

the standard approach LDA/GGA+G_0W_0 are evident. Based on these QP band structures, the optical absorption spectra of rs-CaO, zb-AlN, and wz-AlN have been studied. The calculated dielectric functions including excitonic effects, which have been obtained by solving the BSE, are in very good agreement with recent measured absorption spectra.

The main focus of the paper was to unravel the origin of peaks and structures in the imaginary part of the dielectric function. For this purpose, three complementary methods have been applied: (i) Critical points in the joint band structure were identified and analyzed in terms of their M_0, M_1, M_2, or M_3 character; (ii) spherical regions in **k** space around the high-symmetry points Γ, X, and L have been excluded from the BSE and the resulting changes in the obtained spectra have been evaluated; and (iii) the localization of the excitonic wave function in reciprocal space has been investigated for the low-energy excitations. All three methods yield a widely consistent picture: Some peaks in the absorption spectra can primarily be assigned to bound excitonic states at M_0 or M_1 critical points. Such states do not only occur at the first direct absorption edge, but are also found near higher critical points in resonance with the continuum absorption of the interband transitions. Other peaks cannot be identified with critical points. They are due to a large JDOS in the relevant spectral range with various bands or large parts of the BZ contributing to the absorption. For the materials studied here, a consistent interpretation of most of the spectral peaks has been found which may help experimentalists in interpreting their measurements.

ACKNOWLEDGMENTS

*Current address: Theoretische Physik, Universität Paderborn, Warburger Str. 100, 33098 Paderborn, Germany, riefer@mail.uni-paderborn.de

[1] S. Albrecht, L. Reining, R. Del Sole, and G. Onida, Phys. Rev. Lett. **80**, 4510 (1998).

[2] L. X. Benedict, E. L. Shirley, and R. B. Bohn, Phys. Rev. B **57**, R9385 (1998).

[3] M. Rohlfing and S. G. Louie, Phys. Rev. Lett. **81**, 2312 (1998).

[4] G. Onida, L. Reining, and A. Rubio, Rev. Mod. Phys. **74**, 601 (2002).

[5] L. J. Sham and T. M. Rice, Phys. Rev. **144**, 708 (1966).

[6] W. Hanke and L. J. Sham, Phys. Rev. Lett. **43**, 387 (1979).

[7] G. Strinati, Riv. Nuovo Cimento **11**, 1 (1988).

[8] L. Hedin and S. Lundqvist, in *Solid State Physics. Advances in Research and Applications*, edited by F. Seitz, D. Turnbull, and H. Ehrenreich, Vol. 23 (Academic, New York, 1969), p. 1.

[9] W. G. Aulbur, L. Jönsson, and J. W. Wilkins, in *Solid State Physics. Advances in Research and Applications*, edited by H. Ehrenreich and F. Spaepen, Vol. 54 (Academic, San Diego, 1999), p. 1.

[10] F. Bechstedt, F. Fuchs, and G. Kresse, Phys. Status Solidi B **246**, 1877 (2009).

[11] L. Hedin, Phys. Rev. **139**, A796 (1965).

[12] C. Rödl, F. Fuchs, J. Furthmüller, and F. Bechstedt, Phys. Rev. B **77**, 184408 (2008).

[13] M. Rohlfing and S. G. Louie, Phys. Rev. Lett. **83**, 856 (1999).

[14] P. H. Hahn, W. G. Schmidt, and F. Bechstedt, Phys. Rev. Lett. **88**, 016402 (2001).

[15] M. Palummo, O. Pulci, R. Del Sole, A. Marini, M. Schwitters, S. R. Haines, K. H. Williams, D. S. Martin, P. Weightman, and J. E. Butler, Phys. Rev. Lett. **94**, 087404 (2005).

[16] P. H. Hahn, W. G. Schmidt, K. Seino, M. Preuss, F. Bechstedt, and J. Bernholc, Phys. Rev. Lett. **94**, 037404 (2005).

[17] P. H. Hahn, W. G. Schmidt, and F. Bechstedt, Phys. Rev. B **72**, 245425 (2005).

[18] M. Rohlfing and S. G. Louie, Phys. Rev. Lett. **80**, 3320 (1998).

[19] E. Luppi, F. Iori, R. Magri, O. Pulci, S. Ossicini, E. Degoli, and V. Olevano, Phys. Rev. B **75**, 033303 (2007).

[20] L. E. Ramos, J. Paier, G. Kresse, and F. Bechstedt, Phys. Rev. B **78**, 195423 (2008).

[21] R. Laskowski, N. E. Christensen, G. Santi, and C. Ambrosch-Draxl, Phys. Rev. B **72**, 035204 (2005).

[22] R. Laskowski and N. E. Christensen, Phys. Rev. B **74**, 075203 (2006).

[23] F. Fuchs, C. Rödl, A. Schleife, and F. Bechstedt, Phys. Rev. B **78**, 085103 (2008).

[24] F. Bechstedt, F. Fuchs, and J. Furthmüller, Phys. Status Solidi A **207**, 1041 (2010).

[25] F. Bechstedt, K. Seino, P. H. Hahn, and W. G. Schmidt, Phys. Rev. B **72**, 245114 (2005).

[26] B. Adolph, V. I. Gavrilenko, K. Tenelsen, F. Bechstedt, and R. Del Sole, Phys. Rev. B **53**, 9797 (1996).

[27] W. G. Schmidt, S. Glutsch, P. H. Hahn, and F. Bechstedt, Phys. Rev. B **67**, 085307 (2003).

[28] C. Hamaguchi, *Basic Semiconductor Physics* (Springer, Berlin, 2001).

[29] P. Y. Yu and M. Cardona, *Fundamentals of Semiconductors*, 3rd ed. (Springer, Berlin, 2005).

[30] C. Kittel, *Introduction to Solid State Physics*, 8th ed. (Wiley, Hoboken, NJ, 2005).

[31] A. Schleife, C. Rödl, F. Fuchs, J. Furthmüller, and F. Bechstedt, Phys. Rev. B **80**, 035112 (2009).

[32] A. García and M. L. Cohen, Phys. Rev. B **47**, 4215 (1993).

[33] *Table of Periodic Properties of the Elements* (Sargent-Welch Scientific, Skokie, IL, 1980).

[34] C.-Y. Yeh, Z. W. Lu, S. Froyen, and A. Zunger, Phys. Rev. B **46**, 10086 (1992).

[35] W. Martienssen and H. Warlimont, eds., *Springer Handbook of Condensed Matter and Materials Data* (Springer, Berlin, 2005).

[36] D. J. As, Microelectron. J. **40**, 204 (2009).

[37] P. Hohenberg and W. Kohn, Phys. Rev. **136**, B864 (1964).

[38] W. Kohn and L. J. Sham, Phys. Rev. **140**, A1133 (1965).

[39] G. Kresse and J. Furthmüller, Comput. Mater. Sci. **6**, 15 (1996).

[40] G. Kresse and D. Joubert, Phys. Rev. B **59**, 1758 (1999).

[41] J. P. Perdew, K. Burke, and M. Ernzerhof, Phys. Rev. Lett. **77**, 3865 (1996).

[42] F. D. Murnaghan, Proc. Natl. Acad. Sci. USA **30**, 244 (1944).

[43] J. Heyd, G. E. Scuseria, and M. Ernzerhof, J. Chem. Phys. **118**, 8207 (2003).

[44] F. Fuchs, J. Furthmüller, F. Bechstedt, M. Shishkin, and G. Kresse, Phys. Rev. B **76**, 115109 (2007).

[45] M. Shishkin and G. Kresse, Phys. Rev. B **74**, 035101 (2006).

[46] M. Gajdoš, K. Hummer, G. Kresse, J. Furthmüller, and F. Bechstedt, Phys. Rev. B **73**, 045112 (2006).

[47] F. Bechstedt, R. Del Sole, G. Cappellini, and L. Reining, Solid State Commun. **84**, 765 (1992).

[48] T. Schupp, G. Rossbach, P. Schley, R. Goldhahn, M. Röppischer, N. Esser, C. Cobet, K. Lischka, and D. J. As, Phys. Status Solidi A **207**, 1365 (2010).

[49] M. Ueno, A. Onodera, O. Shimomura, and K. Takemura, Phys. Rev. B **45**, 10123 (1992).

[50] W. A. Harrison, *Elementary Electronic Structure* (World Scientific, Singapore, 1999).

[51] W. A. Harrison, *Electronic Structure and the Properties of Solids* (Dover, New York, 1989).

[52] S. Limpijumnong and W. R. L. Lambrecht, Phys. Rev. B **63**, 104103 (2001).

[53] A. Schleife, F. Fuchs, J. Furthmüller, and F. Bechstedt, Phys. Rev. B **73**, 245212 (2006).

[54] R. C. Whited, C. J. Flaten, and W. C. Walker, Solid State Commun. **13**, 1903 (1973).

[55] M. P. Thompson, G. W. Auner, T. S. Zheleva, K. A. Jones, S. J. Simko, and J. N. Hilfiker, J. Appl. Phys. **89**, 3331 (2001).

[56] M. Röppischer, R. Goldhahn, G. Rossbach, P. Schley, C. Cobet, N. Esser, T. Schupp, K. Lischka, and D. J. As, J. Appl. Phys. **106**, 076104 (2009).

[57] J. Li, K. B. Nam, M. L. Nakarmi, J. Y. Lin, H. X. Jiang, P. Carrier, and S.-H. Wei, Appl. Phys. Lett. **83**, 5163 (2003).

[58] C. Rödl, F. Fuchs, J. Furthmüller, and F. Bechstedt, Phys. Rev. B **79**, 235114 (2009).

[59] A. Yamasaki and T. Fujiwara, Phys. Rev. B **66**, 245108 (2002).

[60] A. Rubio, J. L. Corkill, M. L. Cohen, E. L. Shirley, and S. G. Louie, Phys. Rev. B **48**, 11810 (1993).

[61] P. Rinke, M. Winkelnkemper, A. Qteish, D. Bimberg, J. Neugebauer, and M. Scheffler, Phys. Rev. B **77**, 075202 (2008).

[62] I. Vurgaftman and J. R. Meyer, J. Appl. Phys. **94**, 3675 (2003).

[63] R. J. Elliott, Phys. Rev. **108**, 1384 (1957).

[64] B. Velický and J. Sak, Phys. Status Solidi B **16**, 147 (1966).

[65] E. O. Kane, Phys. Rev. **180**, 852 (1969).

[66] R. C. Whited and W. C. Walker, Phys. Rev. **188**, 1380 (1969).

[67] W. Y. Ching, F. Gan, and M.-Z. Huang, Phys. Rev. B **52**, 1596 (1995).

[68] R. C. Whited and W. C. Walker, Phys. Rev. Lett. **22**, 1428 (1969).

[69] P. H. Hahn, K. Seino, W. G. Schmidt, J. Furthmüller, and F. Bechstedt, Phys. Status Solidi B **242**, 2720 (2005).

[70] G. D. Mahan, Phys. Rev. **153**, 882 (1967).

[71] G. D. Mahan, *Many-Particle Physics*, 2nd ed. (Plenum, New York, 1990).

[72] G. Rossbach *et al.*, Phys. Status Solidi B **247**, 1679 (2010).

[73] L. X. Benedict, T. Wethkamp, K. Wilmers, C. Cobet, N. Esser, E. L. Shirley, W. Richter, and M. Cardona, Solid State Commun. **112**, 129 (1999).

[74] J. Chen, W. Z. Shen, H. Ogawa, and Q. X. Guo, Appl. Phys. Lett. **84**, 4866 (2004).

[75] A. Schleife, J. B. Varley, F. Fuchs, C. Rödl, F. Bechstedt, P. Rinke, A. Janotti, and C. G. Van de Walle, Phys. Rev. B **83**, 035116 (2011).

[76] U. Fano, Phys. Rev. **124**, 1866 (1961).

[77] L. Chen *et al.*, Appl. Phys. Lett. **85**, 4334 (2004).

[78] E. Silveira, J. A. Freitas, O. J. Glembocki, G. A. Slack, and L. J. Schowalter, Phys. Rev. B **71**, 041201 (2005).

[79] G. Rossbach *et al.*, Phys. Rev. B **83**, 195202 (2011).

[80] B. Gil, B. Guizal, D. Felbacq, and G. Bouchitté, Eur. Phys. J. Appl. Phys. **53**, 20303 (2011).